JACS
JOURNAL OF THE AMERICAN CHEMICAL SOCIETY

Article

pubs.acs.org/JACS

Giant Piezoelectricity and High Curie Temperature in Nanostructured Alkali Niobate Lead-Free Piezoceramics through Phase Coexistence

Bo Wu,[†,§,∥] Haijun Wu,[‡,∥] Jiagang Wu,*[,†] Dingquan Xiao,[†] Jianguo Zhu,[†] and Stephen J. Pennycook*[,‡]

[†]Department of Materials Science, Sichuan University, Chengdu 610064, People's Republic of China

[‡]Department of Materials Science and Engineering, National University of Singapore, Singapore 117575, Singapore

[§]Sichuan Province Key Laboratory of Information Materials and Devices Application, Chengdu University of Information Technology, Chengdu 610225, People's Republic of China

Supporting Information

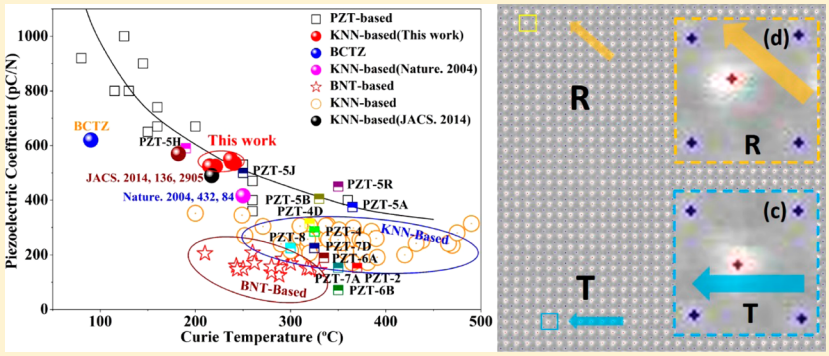

ABSTRACT: Because of growing environmental concerns, the development of lead-free piezoelectric materials with enhanced properties has become of great interest. Here, we report a giant piezoelectric coefficient (d_{33}) of 550 pC/N and a high Curie temperature (T_C) of 237 °C in $(1-x-y)K_{1-w}Na_wNb_{1-z}Sb_zO_3$–$x$BiFeO$_3$–$yBi_{0.5}Na_{0.5}ZrO_3$ (KN_wNS_z-xBF-yBNZ) ceramics by optimizing x, y, z, and w. Atomic-resolution polarization mapping by Z-contrast imaging reveals the intimate coexistence of rhombohedral (R) and tetragonal (T) phases inside nanodomains, that is, a structural origin for the R–T phase boundary in the present KNN system. Hence, the physical origin of high piezoelectric performance can be attributed to a nearly vanishing polarization anisotropy and thus low domain wall energy, facilitating easy polarization rotation between different states under an external field.

INTRODUCTION

Piezoelectric materials interconvert electrical energy into mechanical energy, and are widely used for electronic devices.[1−3] In the past several decades, lead zirconate titanate (PZT) ceramics have dominated the piezoelectric market because of their excellent properties and flexibility in terms of compositional modifications. However, lead-based piezoceramics will be replaced in the future by their lead-free counterparts to protect our surviving environment.[4−6] Recently, much attention has been paid to alkali niobate systems because of their good comprehensive performance.[7−17] In 2004, Saito et al. reported that the Li, Ta, and Sb-modified (K, Na)NbO$_3$ ceramics grown by reactive-templated grain growth show a giant d_{33} of ∼416 pC/N,[3] initiating broad interest. However, KNN-based ceramics still exhibit a poorer piezoelectricity as compared to most of the lead-based ones. Therefore, it is necessary to further enhance the piezoelectric properties of KNN-based ceramics to replace PZT.

Recently, the construction of phase boundaries by the addition of ions or second compounds has become popular to promote the electrical properties of KNN-based ceramics.[3,10,12,17−24] As is known, a d_{33} of <350 pC/N can be observed in the KNN-based ceramics with orthorhombic–tetragonal (O–T) or rhombohedral–orthorhombic (R–O) phase boundaries, which cannot meet the requirements of many electronic devices.[17,24] In 2014, a new KNN-based ceramic material with $d_{33} \approx 490$ pC/N was obtained by designing new phase boundaries consisting of rhombohedral and tetragonal (R–T) phases,[10] indicating that the construction of new phase boundaries is a key factor to determine the piezoelectric properties of KNN-based ceramics.[10,22,23] According to the previous references, composition also strongly affects their piezoelectric properties, raising the question of whether a larger d_{33} (>490 pC/N) together with a high T_C (>220 °C)[10] can be realized by using both composition design and phase boundary modification. In addition, the physical origin for high piezoelectricity of KNN-based ceramics remains unclear.

In this work, we designed a new material system comprising $(1-x-y)K_{1-w}Na_wNb_{1-z}Sb_zO_3$-$x$BiFeO$_3$-$yBi_{0.5}Na_{0.5}ZrO_3$

Received: September 1, 2016
Published: November 17, 2016

DOI: 10.1021/jacs.6b09024
J. Am. Chem. Soc. 2016, 138, 15459−15464

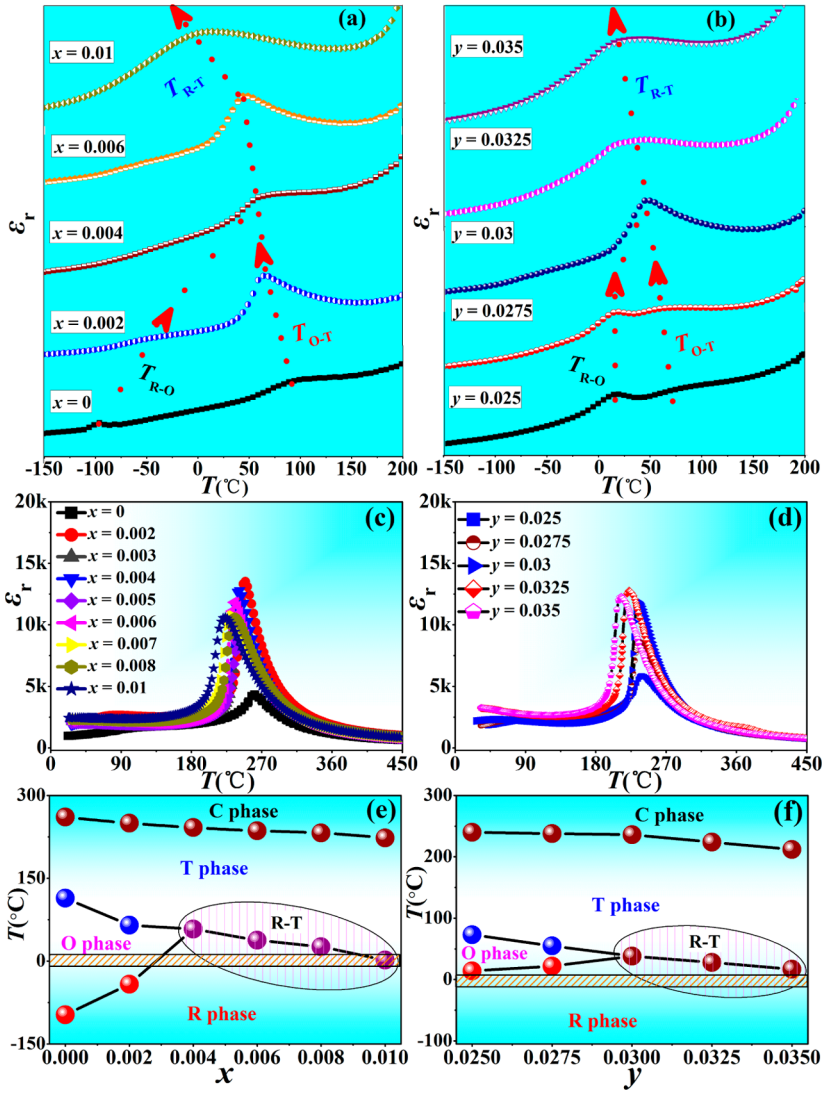

Figure 1. Phase transition of KNNS-*x*BF-*y*BNZ ceramics as a function of *x* and *y*: (a, b) ε_r-T curves from low temperature to room temperature; (c, d) ε_r-T curves from room temperature to high temperature; and (e, f) phase diagrams of KNNS-*x*BF-*y*BNZ ceramics.

(KN_wNS_z-*x*BF-*y*BNZ). Both a giant d_{33} of 550 pC/N and a high T_C of 237 °C were realized by constructing an R−T phase boundary by optimizing *x*, *y*, *z*, and *w*. In addition, through atomic-resolution electron microscopy, we demonstrate the physical origin of such excellent piezoelectric performance.

EXPERIMENTAL SECTION

$(1-x-y)K_{1-w}Na_wNb_{1-z}Sb_zO_3$-$x$BiFeO$_3$-$yBi_{0.5}Na_{0.5}ZrO_3$ ($0 \le x \le 0.01$, $0.025 \le y \le 0.035$, $0.03 \le z \le 0.06$, and $0.40 \le w \le 0.68$) ceramics were prepared by the conventional solid-state reaction process. Na_2CO_3 (99.8%), K_2CO_3 (99%), Bi_2O_3 (99%), Nb_2O_5 (99.5%), Sb_2O_3 (99%), Fe_2O_3 (99%), and ZrO_2 (99%) were used as raw materials. All raw materials of this work were produced by Sinopharm Chemical Reagent Co., Ltd. All of the stoichiometric raw materials were ball milled for 24 h with alcohol as the dispersion medium, and then dried and calcined at 850 °C for 6 h in air. These calcined powders were mixed with a binder of 8 wt % poly vinyl alcohol (PVA) and pressed into the pellets with 10 mm diameter and 1 mm thickness under a pressure of 10 MPa. The PVA was burnt off afterward. All disk samples were sintered at 1085−1100 °C for 3 h in air after the PVA binder was burnt out. All of the samples were polarized in a silicone oil bath at 20 °C under a dc field of 4.0 kV/mm for 20 min.

The phase structure of the sintered cylindrical pellets was identified by X-ray diffraction with Cu Kα radiation (DX-2700, Dandong, China). The capacitance and dissipation factors of the sintered samples were measured using an LCR analyzer (HP 4980, Agilent, U.S.) with temperature varied between −150 to 200 °C and room temperature of ~450 °C. The polarization versus electric field ($P-E$) hysteresis loops of the unpoled cylindrical pellets were measured at 10 Hz with a ferroelectric tester (Radiant Technologies, Inc., Albuquerque, NM). Their planar electromechanical coupling factor (k_p) was measured by a resonance-antiresonance method with an impedance analyzer (Impedance Analyzer, PV70A, Beijing, China). The d_{33} was measured with a commercial Berlincourt-type d_{33} meter (ZJ-3A, China) for the poled samples. Transmission electron microscopy (TEM) and scanning transmission electron microscopy (STEM) were carried out using a JEOL ARM200F atomic-resolution analytical electron microscope equipped with a cold field-emission gun and a new ASCOR fifth-order aberration corrector.

RESULTS AND DISCUSSION

All ceramics are of a pure phase, and no secondary phases are observed in the composition range investigated, indicating that stable solid solutions among KNNS, BNZ, and BF are formed (see Figure S1: XRD patterns of KN_wNS_z-*x*BF-*y*BNZ ceramics). According to the XRD patterns (2θ = 43−47°), we find that mixed phases appear in all ceramics. To further

DOI: 10.1021/jacs.6b09024
J. Am. Chem. Soc. 2016, 138, 15459−15464

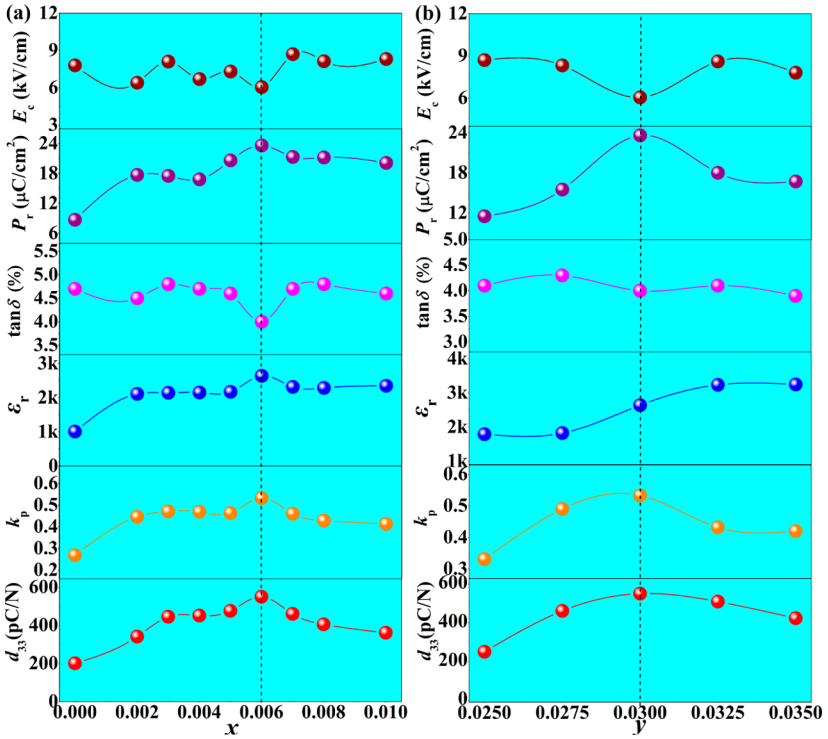

Figure 2. Piezoelectric (d_{33}, k_p), dielectric (ε_r, tan δ), and ferroelectric (P_r, E_c) properties of (a) KNNS-xBF-BNZ and (b) KNNS-BF-yBNZ ceramics.

analyze the compositions of the mixed phases, the ε_r−T (−150 to 200 °C) curves of KNNS-xBF-yBNZ ($0 \le x \le 0.01$, y = 0.006, z = 0.045, w = 0.6; $0.025 \le y \le 0.035$, x = 0.006, z = 0.045, w = 0.6) ceramics are shown in Figure 1a,b. Their T_{O-T} (≥65 °C) and T_{R-O} (≤−42 °C) transition temperatures were found in the ceramics with $x \le 0.002$ (Figure 1a), confirming that they possess an O−T phase boundary. As x increases to 0.004, the two-phase transition peaks (R−O and O−T) converge together to form one R−T peak. One can see that T_{R-T} drops from 58 °C at a BF content of 0.004 to −2 °C at a BF content of 0.010. By using a similar method, we investigated the influences of y, z, and w contents on the phase structure (Figure 1b, Figure S3a−d: ε_r−T curves of KN_wNS_z-BF-BNZ ceramics). Finally, an R−T phase boundary was formed by optimizing the x, y, z, and w. In addition, Rietveld powder diffraction refinement for x = 0.006, y = 0.03, z = 0.045, and w = 0.6 was carried out using the MAUD program,[28,29] showing the coexistence of R and T phases (see Figure S2: Rietveld refinement on XRD patterns of KNNS-BNZ-BF ceramics).

To investigate the effects of x, y, z, and w on T_C, we plot the ε_r−T curves, measured at 20−450 °C and f = 100 kHz (Figure 1c,d, Figure S3c,d: ε_r−T curves of KN_wNS_z-BF-BNZ ceramics). We can see that only one dielectric peak is found in all ceramics, which corresponds to their tetragonal-cubic phase transition temperature (T_C = 190−270 °C).

Figure 1e,f shows the phase diagrams of KNNS-xBF-yBNZ ceramics, established by the data derived from their ε_r−T curves (see Figure 1a−d). Their phase transition temperatures T_{R-O} and T_{O-T} gradually move to room temperature with increasing BF content ($0 \le x < 0.004$), when the R−T phase boundary is formed for x = 0.004, and then with further increase of x (Figure 1e), T_{R-T} decreases. Similar behavior is found for the BNZ and Sb contents (Figure 1f, Figure S3e: phase diagram of $KNNS_z$-BF-BNZ ceramics). In addition, it was also found that the K/Na ratio (w) also affects the phase structure of the ceramics;[25−27] that is, their T_{R-T} increases with increasing w (Figure S3f: phase diagram of KN_wNS-BF-BNZ ceramics). At the same time, their T_C decreases with increasing x, y, and z (Figure 1e,f, Figure S3e: phase diagram of $KNNS_z$-BF-BNZ ceramics), while T_C almost remains unchanged with variations of w (Figure S3f: phase diagram of KN_wNS-BF-BNZ ceramics). As a result, the phase structure of KN_wNS_z-xBF-yBNZ ceramics is defined here: O−T for $0.00 \le x \le 0.002$, R−O−T for $0.002 < x < 0.004$, $0.025 \le y \le 0.0275$, R−T for $0.004 \le x \le 0.01$, $0.0275 < y \le 0.035$, $0.03 \le z \le 0.06$, and $0.4 \le w \le 0.68$.

Figure 2 shows the composition dependence of piezoelectric, dielectric, and ferroelectric properties in the ceramics. One can find that there is a similar change for both d_{33} and k_p, first increasing and then decreasing with the increasing x, y, z, and w, reaching a peak value of $d_{33} \approx 550$ pC/N and $k_p \approx 53.3\%$ for x = 0.006, y = 0.03, z = 0.045, and w = 0.6 (Figure 2, Figure S4: piezoelectric (d_{33}, k_p), dielectric (ε_r, tan δ), and ferroelectric (P_r, E_c) properties of KN_wNS_z-BF-BNZ ceramics). To explore the relationship among dielectric, piezoelectric, and ferroelectric properties, we plot the curves of both $\varepsilon_r P_r$ and d_{33} versus x, y, z, and w (Figure S5: d_{33} and $\varepsilon_r P_r$ of KN_wNS_z-xBF-yBNZ ceramics). All exhibit a similar trend. Both maximum d_{33} and maximum $\varepsilon_r P_r$ could be achieved in the region where the O−T and R−O phase boundaries coexist, implying that enhanced d_{33} may result from the increase of $\varepsilon_r P_r$.[10,13] In addition, their dielectric properties show a strong compositional dependence; that is, ε_r sharply increases for $0 \le x \le 0.002$ and then fluctuates for $0.002 < x \le 0.01$, as shown in Figure 2a. A similar trend in ε_r was also observed in the ceramics with different y contents (see Figure 2b). As for z, their ε_r first increases and then drops for $z > 0.045$, reaching a maximum value for z = 0.045, as w does (Figure S4: piezoelectric (d_{33}, k_p), dielectric (ε_r, tan δ), and ferroelectric (P_r, E_c) properties of KN_wNS_z-BF-BNZ ceramics). In addition, tan δ of all ceramics keeps a

DOI: 10.1021/jacs.6b09024
J. Am. Chem. Soc. 2016, 138, 15459−15464

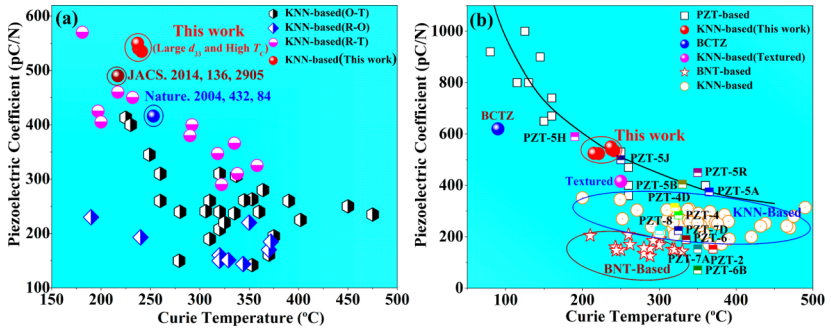

Figure 3. d_{33} as a function of T_C of (a) KNN-based with different phase boundaries, and (b) PZT, BT, BNT, and KNN-based ceramics.

relatively low value of 0.035−0.06 (Figure 2, Figure S4: piezoelectric (d_{33}, k_p), dielectric (ε_r, tan δ), and ferroelectric (P_r, E_c) properties of KN_wNS_z-BF-BNZ ceramics). As a result, optimum dielectric properties ($\varepsilon_r \approx 2641$ and tan $\delta \approx 0.04$) can be obtained in the ceramics with $x = 0.006$, $y = 0.03$, $z = 0.045$, and $w = 0.6$. To further show the variations of ferroelectric properties with x, y, z, and w, their P_r and E_C obtained from their $P-E$ loops are shown in Figures 2 and S4 (Figure S4: piezoelectric (d_{33}, k_p), dielectric (ε_r, tan δ), and ferroelectric (P_r, E_c) properties of KN_wNS_z-BF-BNZ ceramics). We find that a higher P_r and a lower E_C can be simultaneously observed in the R−T phase boundary region ($0.004 \le x \le 0.010$, $0.0275 < y \le 0.035$, $0.03 \le z \le 0.06$, and $0.40 \le w \le 0.68$) because the R−T phase boundary promotes the rotation of polarization vectors.

To clearly compare piezoelectric properties of this work with other reported values, we show both d_{33} and T_C values for other piezoelectric ceramics (Figure 3). One can see that a large d_{33} of 550 pC/N and a high T_C of 237 °C can be attained by careful composition design, and the comprehensive performance of d_{33} and T_C of this work is superior to those of reported KNN-based ceramics regardless of phase boundary types, representing a significant breakthrough (Figure 3a).[1−3,10,13] In addition, such a result is also superior to those of BT and BNT-based lead-free ceramics, and is almost comparable to the best PZT-based ceramics,[1−6] as shown in Figure 3b.

In this work, we attained a high piezoelectricity ($d_{33} \approx 550$ pC/N) in KNN-based ceramics by tuning composition and the location of the R−T phase boundary. To reveal the underlying mechanisms of high piezoelectric performance at the R−T phase boundary, atomic-resolution analytical (S)TEM was employed to characterize the domain morphology and structure. Figure 4a and b shows representative low-magnification TEM bright-field images of ferroelectric domains, observed along [100] and [110] directions. As compared to the traditional microscale herringbone-like or lamellar domains in pure R or T ferroelectric phases,[31,32] the domains at the R−T phase boundary are nanoscale in width, quite similar to those found at the morphotropic phase boundary (MPB) composition in $PbTiO_3$-based and $BaTiO_3$-based systems.[33−35] The electron diffraction patterns inserted in Figure 4a and b exhibit streaking at high-order reflections along the ⟨100⟩ or ⟨110⟩ directions, perpendicular to the elongation direction of the nanodomains in the images. Detailed analysis of the electron diffraction patterns is shown in Figure 4c−h. Three low-index zone axes, [100], [110], and [111], are selected, in which superlattices can be observed (Figure 4c−e) under strong exposure. However, the respective simulated electron diffraction patterns (Figure 4f−h) based on pure R or T phases of KNN only exhibit the main reflections without any superlattice,

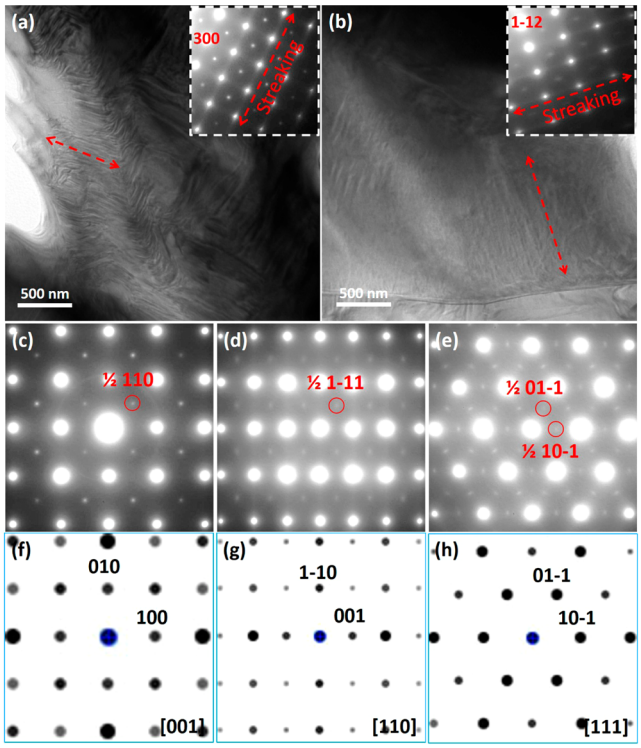

Figure 4. Morphology and diffraction of nanodomains: (a, b) Low-magnification TEM images showing nanodomains; the insets are electron diffraction patterns along [001] and [110] zone axes. The streaking corresponds to the nanodomain elongation direction. (c−e) Experimental electron diffraction patterns along [001], [110], and [111] zone axis, revealing superlattices, which suggest local ordering (symmetry) inside the nanodomains. (f−h) Simulated electron diffraction patterns along [001], [110], and [111] zone axes of KNN, showing no superlattices.

where superlattice here reflects local ordering existing inside the nanodomains. This phenomenon has been widely found in complex perovskite relaxor ferroelectrics, for example, $Pb(Mg_{1/3}Nb_{2/3})O_3$.[42,43]

To further probe into the local crystal ordering or symmetries inside nanodomains, we employed spherical aberration (Cs) corrected STEM to directly observe the atom displacement inside each unit cell, which can convincingly reflect the polarization direction or symmetry.[36,37] Figure 5a is a STEM HAADF (high angle annular dark field) lattice image obtained from a domain boundary. STEM HAADF has been proved to be an effective structure imaging mode especially at the atomic scale, producing contrast interpretable by mass-thickness (the signal is proportional to the number of atoms) or

DOI: 10.1021/jacs.6b09024
J. Am. Chem. Soc. 2016, 138, 15459−15464

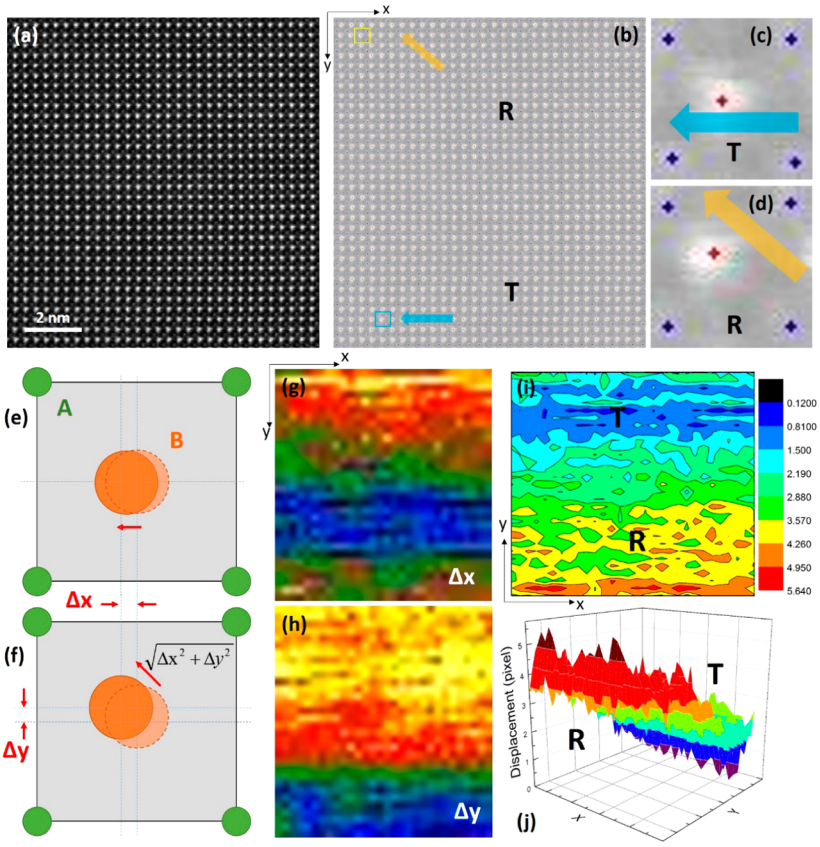

Figure 5. Local symmetry inside nanodomians. (a) STEM HAADF lattice image at a domain boundary; (b) peak finding on (a), revealing R and T regions; (c) enlarged image of the region in (a) within the blue box, showing T symmetry; (d) enlarged image, of the region in (a) within the yellow box, showing R symmetry; (e) schematic showing T symmetry with B (Nb/Sb/Fe/Zr) atom displacement Δx along pseudocubic axes with respect to A (Na/K/Bi) atoms; (f) schematic figure showing R symmetry with B atom displacement along the cube diagonal ($\sqrt{\Delta x^2 + \Delta y^2}$), which can be decomposed into displacements along x and y axes; (g, h) displacement along x and y axes, showing inhomogeneous displacement; the region exhibiting displacement along only one axis reflects T symmetry, while the region exhibiting displacement along both x and y axes reflects R symmetry; and (i, j) 2D and 3D images showing displacement along diagonal direction ($\sqrt{\Delta x^2 + \Delta y^2}$) reflecting different regions with T and R symmetries.

Z contrast (the signal is roughly proportional to the atomic number squared).[38,43,44] The center and corner atoms of the perovskite ABO_3 lattice structure can be easily differentiated through the Z-contrast difference between A and B. In the present sample, the center B site atoms (Nb) are much heavier than the corner A site atoms (Na/K); thus the brighter spots are center atom columns (Figure 5a). To accurately locate the position of each atom column, the peak finder method was used,[39] as shown in Figure 5b. Figure 5c and d shows enlarged areas from Figure 5b, showing that the displacement direction of the center atoms with respect to the corners is different; one is along ⟨100⟩, while the other is along ⟨111⟩. Figure 5e and f shows schematic figures of the T and R unit cells with the center atom displacements along ⟨100⟩ and ⟨111⟩, respectively, consistent with the experimental observations. As the position of each atom column has been identified in Figure 5b, the magnitude of the projected displacement can be calculated via the position difference, as shown in Figure 5g–j. The calculated displacements along x and y axes of the whole area are shown in Figure 5g and h: the region exhibiting displacement along only one axis (Δx or Δy) reflects T symmetry, while the region exhibiting displacement along both x and y axes (Δx and Δy) reflects R symmetry. Figure 5i and j shows 2D and 3D images with the displacement of $\sqrt{\Delta x^2 + \Delta y^2}$, differentiating regions of T symmetry (smaller $\sqrt{\Delta x^2 + \Delta y^2}$ values) from those of R symmetry (larger $\sqrt{\Delta x^2 + \Delta y^2}$ values).

It is evident that the local symmetries inside the nanodomains represent the coexistence of R and T phases, which is quite similar to the case of the MPB composition in lead-based, and the $BaTiO_3$-based/$BiFeO_3$-based lead-free systems.[33,34,36,40] We believe the structural origin of all piezoelectric materials with the composition at R–T phase boundary is such nanodomains with phase coexistence. Derived from such nanoscale/atomic-scale structural coexistence, the physical origin of the high piezoelectric performance of the present KNN system at the R–T phase boundary can therefore be attributed to a nearly vanishing polarization anisotropy and thus low domain wall energy, which facilitates easy polarization rotation between different states under an external field.[30,41]

CONCLUSION

We systematically studied the physical origin of giant piezoelectricity ($d_{33} \approx 550$ pC/N) for $(1-x-y)$-$K_{1-w}Na_wNb_{1-z}Sb_zO_3$-$x$BiFeO$_3$-$yBi_{0.5}Na_{0.5}ZrO_3$ ceramics. Such a good comprehensive performance in nontextured KNN-based ceramics is attributed to nearly vanishing polarization anisotropy and thus low domain wall energy. This discovery is a successful example of piezoelectricity enhancement using phase engineering. We believe that it will certainly be of great

DOI: 10.1021/jacs.6b09024
J. Am. Chem. Soc. 2016, 138, 15459–15464

value for further exploration of high performance lead-free piezoceramics.

■ ASSOCIATED CONTENT

Supporting Information

The Supporting Information is available free of charge on the ACS Publications website at DOI: 10.1021/jacs.6b09024.

Supporting sintering temperatures, XRD patterns, ε_r-T curves, and properties of KN_wNS_z-BF-BNZ ceramics (PDF)

■ AUTHOR INFORMATION

Corresponding Authors

*wujiagang0208@163.com, msewujg@scu.edu.cn

*steve.pennycook@nus.edu.sg

Author Contributions

‖B.W. and H.W. contributed equally.

Notes

The authors declare no competing financial interest.

■ ACKNOWLEDGMENTS

We gratefully acknowledge support from the National Science Foundation of China (NSFC nos. 50972095, 51272164, 51332003, and 51472169).

■ REFERENCES

(1) Uchino, K. *Ferroelectric Devices*; CRC: New York, 2000.

(2) Jaffe, B.; Cook, W. R., Jr.; Jaffe, H. *Piezoelectric Ceramics*; Academic: New York, 1971.

(3) Saito, Y.; Takao, H.; Tani, T.; Nonoyama, T.; Takatori, K.; Homma, T.; Nagaya, T.; Nakamura, M. *Nature* **2004**, *432*, 84.

(4) Shrout, T. R.; Zhang, S. J. *J. Electroceram.* **2007**, *19*, 111.

(5) Rödel, J.; Jo, W.; Seifert, K. T. P.; Anton, E. M.; Granzow, T.; Damjanovic, D. *J. Am. Ceram. Soc.* **2009**, *89*, 1153.

(6) Wu, J. G.; Xiao, D. Q.; Zhu, J. G. *Chem. Rev.* **2015**, *115*, 2559.

(7) Park, S. E.; Shrout, T. R. *IEEE Trans. Ultrason. Ferroelectr. Freq. Control* **1997**, *44*, 1140.

(8) Takenaka, T.; Nagata, H. *J. Eur. Ceram. Soc.* **2005**, *25*, 2693.

(9) Rödel, J.; Kounga, A. B.; Weissenberger-Eibl, M.; Koch, D.; Bierwisch, A.; Rossner, W.; Hoffmanne, M. J.; Danzerf, R.; Schneider, G. *J. Eur. Ceram. Soc.* **2009**, *29*, 1549.

(10) Wang, X. P.; Wu, J. G.; Xiao, D. Q.; Zhu, J. G.; Cheng, X. J.; Zheng, T.; Zhang, B. Y.; Lou, X. J.; Wang, X. J. *J. Am. Chem. Soc.* **2014**, *136*, 2905.

(11) Li, J. F.; Wang, K.; Zhu, F. Y.; Cheng, L. Q.; Yao, F. Z. *J. Am. Ceram. Soc.* **2013**, *96*, 3677.

(12) Guo, Y.; Kakimoto, K.; Ohsato, H. *Appl. Phys. Lett.* **2004**, *85*, 4121.

(13) Xu, K.; Li, J.; Lv, X.; Wu, J. G.; Zhang, X. X.; Xiao, D. Q.; Zhu, J. G. *Adv. Mater.* **2016**, *28*, 8519.

(14) Zhang, S. J.; Xia, R.; Hao, H.; Liu, H. X.; Shrout, T. R. *Appl. Phys. Lett.* **2008**, *92*, 152904.

(15) Zuo, R. Z.; Rödel, J.; Chen, R. Z.; Li, L. T. *J. Am. Ceram. Soc.* **2006**, *89*, 2010.

(16) Matsubara, M.; Yamaguchi, T.; Kikuta, K.; Hirano, S. *Jpn. J. Appl. Phys.* **2005**, *44* (Part 1), 6136.

(17) Wu, J. G.; Xiao, D. Q.; Wang, Y. Y.; Zhu, J. G.; Wu, L.; Jiang, Y. H. *Appl. Phys. Lett.* **2007**, *91*, 252907.

(18) Gao, Y.; Zhang, J. L.; Qing, Y. L.; Tan, Y. Q.; Zhang, Z.; Hao, X. P. *J. Am. Ceram. Soc.* **2011**, *94*, 2968.

(19) Zuo, R. Z.; Fu, J. *J. Am. Ceram. Soc.* **2011**, *94*, 1467.

(20) Wang, K.; Li, J. F. *Adv. Funct. Mater.* **2010**, *20*, 1924.

(21) Wu, J. G.; Wang, Y. Y.; Xiao, D. Q.; Zhu, J. G.; Pu, Z. *Appl. Phys. Lett.* **2007**, *91*, 132914.

(22) Zhang, B. Y.; Wu, J. G.; Cheng, X. J.; Wang, X. P.; Xiao, D. Q.; Zhu, J. G.; Wang, X. J.; Lou, X. J. *ACS Appl. Mater. Interfaces* **2013**, *5*, 7718.

(23) Cheng, X. J.; Wu, J. G.; Wang, X. P.; Zhang, B. Y.; Lou, X. J.; Wang, X. J.; Xiao, D. Q.; Zhu, J. G. *ACS Appl. Mater. Interfaces* **2013**, *5*, 10409.

(24) Mgbemere, H. E.; Hinterstein, M.; Schneider, G. A. *J. Am. Ceram. Soc.* **2013**, *96*, 201.

(25) Wu, L. J.; Zhang, L. C.; Wang, L. J.; Li, C. *J. Appl. Phys.* **2008**, *103*, 084116.

(26) Dai, Y. J.; Zhang, X. W.; Chen, K. P. *Appl. Phys. Lett.* **2009**, *94*, 042905.

(27) Wu, J. G.; Xiao, D. Q.; Wang, Y. Y.; Zhu, J. G.; Wu, L. *Appl. Phys. Lett.* **2007**, *91*, 252907.

(28) Mgbemere, H. E.; Hinterstein, M.; Schneider, G. A. *J. Eur. Ceram. Soc.* **2012**, *32*, 4341.

(29) Fancher, C. M.; Jo, W.; Rödel, J.; Blendell, J. E.; Bowman, K. J. *J. Am. Ceram. Soc.* **2014**, *97*, 2557.

(30) Liu, W. F.; Ren, X. B. *Phys. Rev. Lett.* **2009**, *103*, 257602.

(31) Wu, H. J.; Xue, D. Z.; Lv, D. C.; Gao, J. H.; Guo, S. W.; Zhou, Y. M.; Ding, X. D.; Zhou, C.; Yang, S.; Yang, Y. D.; Ren, X. B. *J. Appl. Phys.* **2012**, *112*, 052004.

(32) Schönau, K. A.; Schmitt, L. A.; Knapp, M.; Fuess, H.; Eichel, R. A.; Kungl, H.; Hoffmann, M. J. *Phys. Rev. B: Condens. Matter Mater. Phys.* **2007**, *75*, 184117.

(33) Gao, J. H.; Xue, D. Z.; Wang, Y.; Wang, D.; Zhang, L. X.; Wu, H. J.; Guo, S. W.; Bao, H. X.; Zhou, C.; Liu, W. F.; Hou, S.; Xiao, G.; Ren, X. B. *Appl. Phys. Lett.* **2011**, *99*, 092901.

(34) Zhang, Y.; Xue, D. Z.; Wu, H. J.; Ding, X. D.; Lookman, T.; Ren, X. B. *Acta Mater.* **2014**, *71*, 176.

(35) Wang, H.; Zhu, J.; Lu, N.; Bokov, A. A.; Ye, Z. G.; Zhang, X. W. *Appl. Phys. Lett.* **2006**, *89*, 2908.

(36) Zeches, R. J.; Rossell, M. D.; Zhang, J. X.; Hatt, A. J.; He, Q.; Yang, C. H.; Kumar, A.; Wang, C. H.; Melville, A.; Adamo, C.; Sheng, Y.; Chu, G. H.; Ihlefeld, J. F.; Erni, R.; Ederer, C.; Gopalan, V.; Chen, L. Q.; Schlom, D. G.; Spaldin, N. A.; Martin, L. W.; Ramesh, R. *Science* **2009**, *326*, 977.

(37) Tang, Y. L.; Zhu, Y. L.; Ma, X. L.; Borisevich, A. Y.; Morozovska, A. N.; Eliseev, E. A.; Wang, W. Y.; Wang, Y. J.; Xu, Y. B.; Zhang, Z. D.; Pennycook, S. J. *Science* **2015**, *348*, 547.

(38) Pennycook, S. J.; Boatner, L. A. *Nature* **1988**, *336*, 565.

(39) Gong, Y. J.; Liu, Z.; Lupini, A. R.; Shi, G.; Lin, J.; Najmaei, S.; Lin, Z.; Elías, A. L.; Berkdemir, A.; You, G.; Terrones, H.; Terrones, M.; Vajtai, R.; Pantelides, S. T.; Pennycook, S. J.; Lou, J.; Zhou, W.; Ajayan, P. M. *Nano Lett.* **2014**, *14*, 442.

(40) Zhang, J. X.; Xiang, B.; He, Q.; Seidel, J.; Zeches, R. J.; Yu, P.; Yang, S. Y.; Wang, C. H.; Chu, Y. H.; Martin, L. W.; Minor, A. M.; Ramesh, R. *Nat. Nanotechnol.* **2011**, *6*, 98.

(41) Rossetti, G. A., Jr; Zhang, W.; Khachaturyan, A. G. *Appl. Phys. Lett.* **2006**, *88*, 072912.

(42) Miao, S.; Zhu, J.; Zhang, X. W.; Cheng, Z. Y. *Phys. Rev. B: Condens. Matter Mater. Phys.* **2001**, *65*, 05210.

(43) Pennycook, S. J. *Ultramicroscopy* **1989**, *30*, 58.

(44) Pennycook, S. J.; Jesson, D. E. *Phys. Rev. Lett.* **1990**, *64*, 938.

DOI: 10.1021/jacs.6b09024
J. Am. Chem. Soc. 2016, 138, 15459−15464